Zhengmao Yang[1]
Mem. ASME
Associate Professor
Institute of Mechanics,
Chinese Academy of Sciences,
Beijing 100190, China;
School of Engineering Science,
University of Chinese Academy of Sciences,
Beijing 100049, China
e-mail: zmyang@imech.ac.cn

Keji Pang
China Academy of Launch Vehicle Technology,
Beijing 100076, China
e-mail: pkj528@126.com

Xianqi Lei
Institute of Mechanics,
Chinese Academy of Sciences,
Beijing 100190, China
e-mail: leixianqi@imech.ac.cn

Qing Hu
State Key Laboratory of Silicate Materials for Architectures,
Wuhan University of Technology,
Wuhan 430070, China
e-mail: huqing09@whut.edu.cn

A Quantitative Representation of Damage and Failure Response of Three-Dimensional Textile SiC/SiC Ceramics Matrix Composites Subjected to Flexural Loading

In the present work, the microstructure deformation and synergetic damage evolution of a three-dimensional textile SiC/SiC ceramic-matrix composite under flexural loading are investigated by in situ digital image correlation at ambient temperatures. The correlations between microstructure evolution and macro-mechanical degradation of 3D textile composites under flexural loading are established based on the experimental results. In addition, by establishing continuum damage mechanics and a thermodynamic framework with synergetic effects of microstructures, a flexural loading-induced damage evolution model is developed to reveal the relationship between the energy release rate and elastic modulus degradation. The proposed model can be used to predict the flexural stress–strain curves of 3D textile SiC/SiC composites to further improve the design and assessment of new textile architectures with specific mechanical properties. [DOI: 10.1115/1.4056414]

Keywords: ceramic matrix composites, silicon carbide, mechanical behavior, microstructure deformation, damage modeling/model, flexural loading

1 Introduction

Fiber-reinforced SiC/SiC ceramic-matrix composites (CMCs) offer an excellent combination of thermomechanical properties and superior physical/chemical properties at high temperatures, such as low density, high strength and toughness, chemical inertness, creep resistance, and irradiation tolerance [1–4]. These superior properties make SiC/SiC composites beneficial for high-temperature structural applications that are exposed to extreme environments, such as hot components in gas turbine engines [5,6], thermal protection systems for advanced vehicles [7], and nuclear reactors [8]. After approximately three decades of development, the investigation of CMCs is still far from a closed topic despite remarkable technological advances. The heterogeneity, architecture, and multiscale structure of CMCs, the complexity of damage mechanisms, including both physical and chemical phenomena, and the inherent randomness of brittle element components need in-depth studies to provide insightful knowledge for the development and application of CMCs [9–12].

Many researchers have focused on the mechanical behaviors of SiC/SiC composites subjected to tensile or compressive loads [13,14], under which conditions the principal stresses are aligned with the fiber axes. These investigations prove that the damage mechanisms that cause the inelastic behaviors of CMCs are matrix cracking, fiber breakage, and delamination [15–18]. However, when the material structure is subjected to bending loads, the stress state and the mechanical behavior of materials are more complex than those under uniaxial loads. Furthermore, tensile/compressive and shear stresses will be induced in the materials, and the principal stresses may not be aligned with the fiber axes, both of which influence the macroscopic behavior of CMCs [19,20]. Consequently, investigation of the flexural behavior of the CMCs and quantitative description of the flexural loading-induced damage mechanism become important for the application of such composites.

The works on the bending loading of textile composites have been rarely reported, and most of them are experimental work. Hild et al. [21] investigated the fracture of CMCs under bending loading, and a predictive model was established to capture the influence of inelasticity based on fiber fragmentation theory. McNulty and Zok [22] suggest that the strength and reliability of CMCs depend on the condition of local or global load sharing. Zhang et al. [23,24] investigated the deformation response of 3D textile composites through flexural tests and developed a multiscale mechanics-based model for the deformation, damage, and failure response of 3D textile composites under flexural loading. Yang et al. [25] developed a progressive damage model to describe the flexural and damage behavior for laminated composites under three-point bending. Chao et al. [26] implemented simulations on 2D cross-ply C/C composites under bending loading, and the ultimate bending strength was obtained using the progressive damage criterion. Wan et al. [27] investigated the damage development within three-dimensional five-directional braided C/C-SiC composites during in situ flexural tests, and they demonstrated that internal cracking leads to a decrease in the elastic modulus. Pirzada et al. [28] observed the deformation and fracture behavior of oxide/oxide CMCs under flexural stress conditions at ambient temperature and 1100 °C, using in situ synchrotron X-ray computed microtomography. Liu et al. [29] also used X-ray computed microtomography to study the failure condition of 3D four-step braided SiC/SiC composites under flexural loading. In summary, the investigations of the degradation of the materials under flexural loading are limited to experimental data and qualitative analysis. There is lack of dependable models to quantitatively describe the mechanical response and progressive damage behavior of CMCs under flexural loading.

Numerous studies have utilized digital image correlation (DIC) to understand the mechanical behavior of fiber-reinforced composites. Rajan et al. [30] measured the inhomogeneous strain field of the

[1]Corresponding author.

Contributed by the Materials Division of ASME for publication in the Journal of Engineering Materials and Technology. Manuscript received August 26, 2022; final manuscript received November 29, 2022; published online December 26, 2022. Assoc. Editor: Francis Aviles-Cetina.

eight-harness satin weave SiC/SiC using full-field displacement mapping techniques, and the correlation between the underlying weave features and the strain distribution was investigated. Gonabadi et al. [31–33] studied the effect of ply orientation on the tensile/shear properties and failure modes of woven glass fiber-reinforced polymer composites although a combined method of finite element analysis, DIC, and microscopy. Full-field strain maps obtained by the DIC method were used to evaluate the damage development and the inhomogeneity of strain localization. Bumgardner et al. [34] quantified the crack opening displacement as well as the flexural strain of SiC/SiC CMCs using in situ stereoscopic DIC technology. These studies demonstrate the suitability of DIC for measuring local strains with high accuracy and spatial resolution in woven fiber composites.

In the present work, the mechanical response behavior and its synergetic damage evolution in 3D textile SiC/SiC composites subjected to flexural loading are investigated. Correlations between microstructure evolution and macro-mechanical degradation are revealed based on the combined DIC analysis and scanning electron microscopy (SEM) microstructure observation. Microstructure-based crack initiation and propagation and its driving mechanism are shown to be linked to the 3D textile architecture of composites; hence, a novel flexural loading-induced synergetic damage evolution model is developed based on continuum damage mechanics (CDM) and the framework of thermodynamics, and the predicted results are compared with experimental results to verify the veracity of the proposed model. This model can be implemented in a finite element program directly for structural analysis and thus can be applied to design composites with 3D textile architecture with specific mechanical properties.

2 Materials and Experiments

2.1 Materials and Specimens. In this work, the investigated 3D textile SiC/SiC CMCs are prepared by the precursor infiltration pyrolysis (PIP) process. Second-generation SiC fibers (KD-II) are woven into 3D reinforcement based on the mechanical design model. Then, chemical vapor deposition was applied to the SiC fiber surface to generate a PyC protective layer with a deposition temperature of 950 °C and a deposition time of 60 min [35]. Subsequently, liquid polycarbosilane was selected as the precursor to conduct 10 cycles of impregnation-pyrolysis until the weight gain rate was less than 1%. The final bulk density of the SiC/SiC CMCs is 2.12 g/cm^3, and the fiber volume fraction is approximately 47.4%.

The woven architecture of the materials is shown in Fig. 1(*a*), which has an eight-harness satin weave consisting of warp and weft tows. The warp yarn is interwoven with the weft yarn by bending and undulating in the thickness direction, resulting in remarkable in-plane mechanical properties. More importantly, the fabric is layered in the thickness direction, and *Z*-fiber is introduced to suture the fabric up and down along the thickness direction and perpendicular to the warp and weft yarn, thus forming a *Z*-direction enhanced 3D structure (Fig. 1(*b*)).

The materials fabricated by the PIP process possess excellent mechanical properties. The low reaction temperature causes less damage to the fibers to a certain degree. Nevertheless, because of the inadequate penetration of precursors and gas escape during pyrolysis, the open porosity of the SiC/SiC CMCs is up to 3.67%.

Three-dimensional visualization of the investigated composites is achieved through X-ray computed tomography (Phoenix v|tome|x m X-ray CT System, GE). The system is capable of generating 3D tomograms at a sufficiently high spatial resolution of 4.7 μm per voxel to image structural details at the microscale. The source voltage and current in the present in situ test are 120 KV and 40 μA, respectively. The exposure time is up to 500 ms, and the scanning area size is 7.5 mm × 5.0 mm × 4.2 mm. A full 3D volume set of the specimen was created by stacking together 1000 projection images, and the final datasets were analyzed. Figure 2 illustrates the microstructure of the 3D textile SiC/SiC CMCs observed by 3D X-ray tomography visualization. It is noted that the SiC fiber and SiC matrix have similar thresholds in the 2D image slices, and the warp and weft fiber bundles are expressed as green and purple in the figure, respectively. The black region shown in Figs. 2(*b*) and 2(*c*) represent the matrix in the composites.

To conduct the three-point bend flexure experiments, a surface grinder equipped with a diamond saw blade was utilized to cut the SiC/SiC composite plate into strips. The specimens should be polished using successive diamond polishing compounds of 6 μm, 3 μm, and a final polish of 1 μm to avoid defects on the surface of the samples, resulting in the dispersion or failure of the test results.

2.2 Three-Point Bend Flexure Experiments. Three-point bend flexure experiments of the 3D textile SiC/SiC CMCs were conducted on an MTS electronic universal testing machine, and the force measurement range of the machine was ±100 kN. The experiments are proceeded under displacement control at a cross-hand speed of 0.5 mm/min following ASTM C1341-13 [36]. The load configuration of the three-point bend flexure experiments is demonstrated in Fig. 3. After the experiments, the fracture surfaces and microstructures of the damaged specimens were examined using SEM.

The specimens for the tests have a size of 60 mm × 10 mm × 5 mm. To obtain the speckle used for DIC observation, the surfaces in the direction of specimen thickness were first coated with white

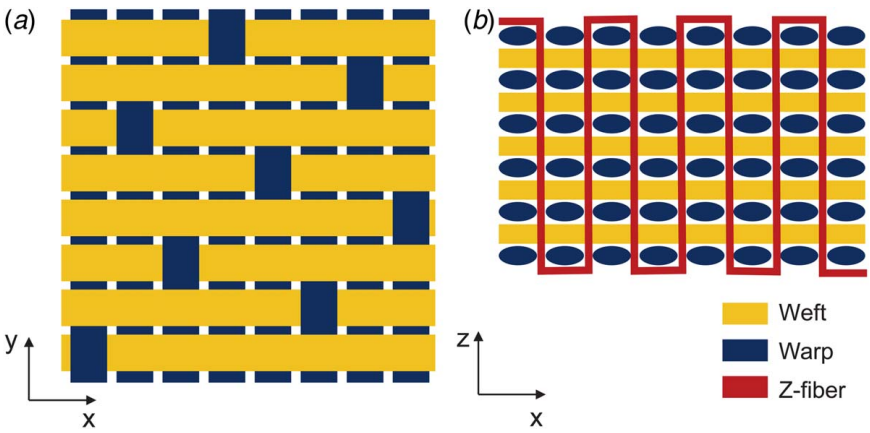

Fig. 1 (*a*) The textile architecture of the 3D textile SiC/SiC CMCs and (*b*) *Z*-fiber is introduced to suture the fabric up and down along the thickness direction and perpendicular to the warp and weft yarn

spray paint and then black spray paint. The strain of the specimens is recorded by the double-digital camera DIC. The displacement of the specimens recorded by a CCD resolution of 3376 × 2704 pixels is obtained.

The focal length of the lenses was 75 mm, and the angle between cameras was 22 deg. The frame rate of the camera is 10 fps. It is worth noting that for all experiments in this work, either the maximum/minimum focal length was utilized to minimize errors arising from differences in magnification between the two CCD cameras. Then, the images for DIC are disposed of by the software VIC-3D (correlated solutions).

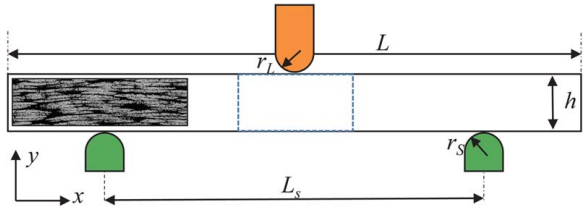

Fig. 3 The load configuration of the three-point bend flexure experiments; the region represented by the dashed line is the region of interest for DIC analysis. Here, the supporting span, L_S, is 50 mm, and both the load nose radius, r_L, and the support radius, r_S, are 2 mm.

3 Mechanical Characterization and Microstructure Damage Mechanism

3.1 Microstructure Progressive Damage Mechanism Analysis. To investigate the damage mechanism of the SiC/SiC composites under three-point flexural loading, a large number of detailed SEM observations were performed, and representative SEM micrographs of a SiC/SiC composite (failure specimen) cross section are shown in Fig. 4. Different from 2D woven composites, the *Z*-pin fibers have a significant influence on the flexural properties of SiC/SiC CMCs. The matrix crack propagates in matrix enrichment regions perpendicular to the fiber tows, with local deflection near the fiber/matrix interface surfaces; its propagation is diffused into sinuous fractures and presents the elements of a *H-Shaped* path, as illustrated in Fig. 4(*a*). These progressive damage processes dissipate the strain energy of the composites. The *Z*-pin fiber strengthens the out-of-plane properties of the material and improves the ability of the material to resist delamination to some extent, which has been observed by some researchers [29,37,38]. The ultimate failure of the specimen is caused by the damage extended from the compressive to the tensile surface, and the specimen cannot sustain the applied loading.

Some typical kinds of damage and failure mechanisms can be observed on both the tensile and compressive sides. At the compressive side, the loading pin causes the local stress concentration, which further leads to *crack propagation* and *fiber debonding*. In addition, the transverse compression of the fiber bundles causes *shear fracture*, as presented in Fig. 4(*b*). Moreover, with the compressive stress increase, *debonding* occurs at the interface of the fiber and matrix and extends to the tensile side, developing further under flexural loading that causes *delamination*; and it was identified in Fig. 4(*a*).

On the tensile side, microstructure damage was initiated near the tensile surface as the load increased. The normal tensile stress leads to *matrix cracks* occurring from the tensile side. When the loading increases, the cracks will propagate to the fiber bundles, resulting in a *fiber pull-out*, as shown in Figs. 4(*c*) and 4(*d*). The fracture surface is perpendicular to the fiber axis direction; in this process, the inelastic strain caused by matrix cracking and fiber pull-out contributes to stress redistribution.

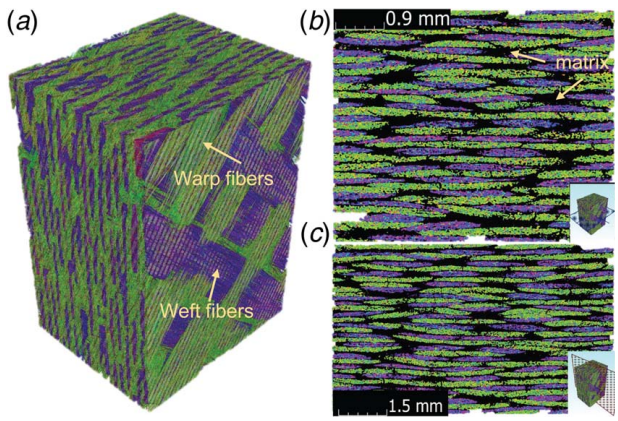

Fig. 2 Microstructure of the 3D textile SiC/SiC CMCs observed by 3D X-ray tomography visualization. Dark and light represent the weft fibers and warp fibers, respectively.

In general, fiber breaking occurs on the tensile side, and fiber shearing or buckling is induced from the compressive side. The matrix cracking and interface debonding are distributed on both the tensile and compressive sides. Among these damages, interface debonding notably affects the flexural properties of materials; thus, it is important to take into account the interface debonding properties when designing CMC components suffering flexural loading. A schematic illustration of the damage sequence can be observed in Fig. 5. Due to the stress concentration caused by the loading pin, crack nucleation arises in the compressive side of the specimen, as shown in Fig. 5(*a*). With the loading increases, the cracks propagate from the highest shear location, and there are some matrix cracks and delamination in the stress concentration location; then, the cracks diffuse into sinuous fractures and present the elements of a *H-Shaped* path, as illustrated in Fig. 5(*c*).

3.2 Mechanical Characterization. The flexure stress σ_f and flexure strain ε_f are defined as the stress and strain at the midpoint of the outer surface, respectively. Since the ratio of the maximum bending deflection δ_M and support span L is less than 0.1 during the bending process, $\delta_M/L \leq 0.1$; the flexural stress σ_f and flexure strain can be calculated by the following equation:

$$\sigma_f = \frac{3}{2}\frac{PL}{bh^2}, \quad \varepsilon_f = 6\frac{\Delta h}{L^2} \tag{1}$$

where P is the reaction force corresponding to the displacement load applied at the reference point, Δ is the displacement, and h and b are the thickness and width of the specimen, respectively.

The flexural elastic modulus E_B is expressed as

$$E_B = \frac{mL^3}{4bh^3} \tag{2}$$

where m represents the slope of the initial linear part of the load–displacement curves. Table 1 shows the flexure mechanical properties of the SiC/SiC CMC specimens for each specimen tested.

The typical flexure stress–strain curves of the composites are illustrated in Fig. 6. The average ultimate flexure strength and strain of the composites are 322 ± 12 MPa and $0.70 \pm 0.07\%$, respectively, with an elastic modulus of 53.5 ± 4.5 GPa. The response of the composite under monotonic flexure loading shows a first nonlinear segment and a second quasi-linear segment. The first nonlinear segment appears in the elastic region of the material, which is caused by the coupling interaction between the settling or slipping in the fixture and an initial ramp up of the initial testing velocity. Thus, the first nonlinear segment does not represent properties of the composites. At the beginning of loading, the initial damage occurs on the tensile surface, and the stress–strain curves show nonlinear behavior and gradually become quasi-linear after the strain at 0.001. Inelastic strain

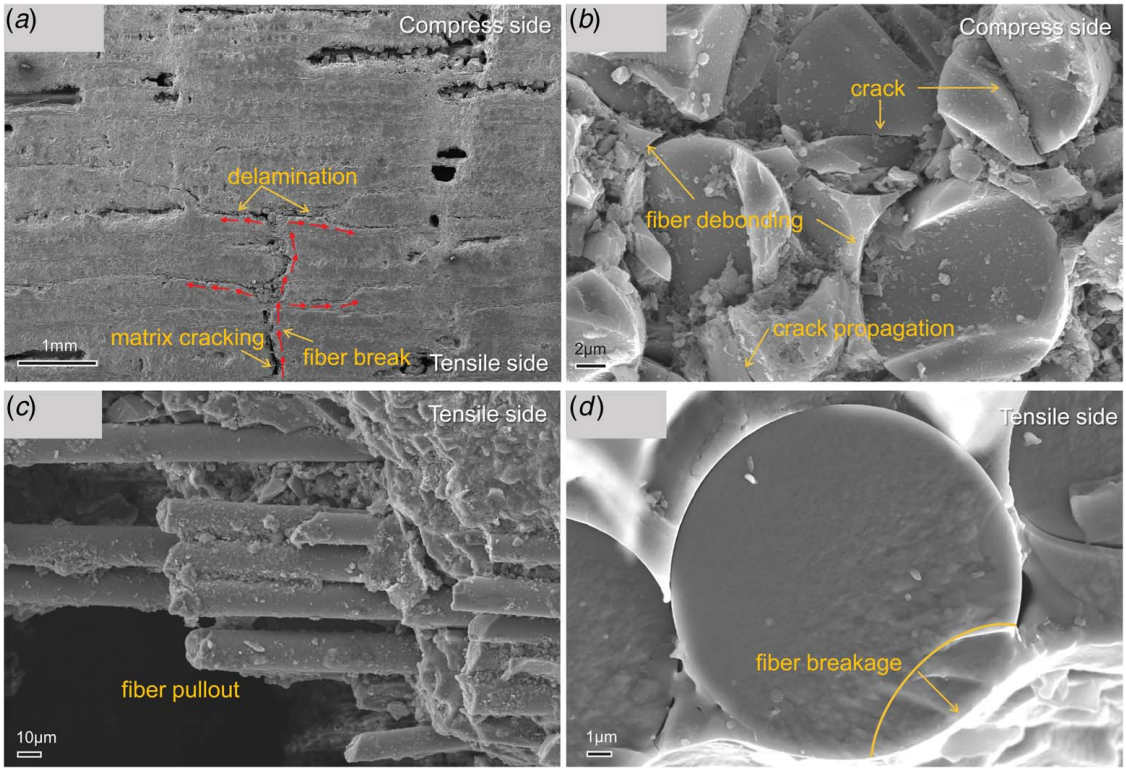

Fig. 4 (*a*) SEM micrograph of a polished SiC/SiC composite (failure specimen) cross section, (*b*) fiber debonding and crack propagation in fracture surfaces of the compress side, (c) fiber pull-out in fracture surfaces of the tensile side, and (*d*) fracture origins in partially fibers associated with tensile stress (indicated by arrows)

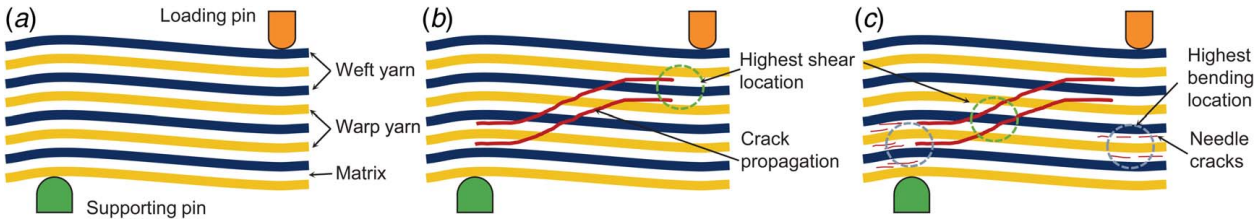

Fig. 5 Schematic illustration of the damage sequence of the SiC/SiC CMCs under three-point flexural loading: (*a*) crack nucleation, (*b*) crack propagation at the highest shear location, and (c) crack progressive propagation driven by shear stress and the needle cracks present at the highest bending moment location

associated with matrix cracking and fiber fragmentation leads to stress redistribution. More essentially, the failure occurs at the end of the second quasi-linear segment, and a drop occurs when the flexure strength is reached. This phenomenon is caused by the brittle fracture of the bearing warp dragged on the compression side of the specimens.

In addition, the stress–strain curves and the damage failure mechanisms for these specimens show similar tendencies; for the sake of simplification, a typical sample S1 is taken into consideration in the present work.

Table 1 Measured flexure mechanical properties of the SiC/SiC CMC specimens

Specimen num.	Flexure modulus (GPa)	Failure stress (MPa)	Failure strain (%)
Sample 1 (S1)	55.32	310.23	0.635
Sample 2 (S2)	56.22	322.07	0.704
Sample 3 (S3)	49.01	334.93	0.781

It should be emphasized that in contrast to the literature [28,29], the flexural strength σ_u of the present work is defined as the strength when the effective bearing capacity of the specimen drops suddenly, instead of the strength σ_{frac} when the specimen is completely fractured. The reason is that SiC/SiC CMCs are quasi-elastic brittle materials, and the strength at the final fracture often presents the characteristics of random probability; thus, σ_{frac} is not the needed design value when designing CMC components, which is extremely important to achieve this result.

Figure 7 demonstrates the displacement fields of the specimen in the *XY* plane under different loadings, which are generated by DIC. It shows the typical characteristics of three-point bending, and the bending center is marked by dotted lines, which is the location of the loading pin.

In addition, the strain fields can be generated by the displacement fields, and Fig. 8 shows the distribution of the normal stress ε_{xx} perpendicular to the cross section with increasing flexural stress. The strain distribution represents a clearly nonuniform field (Fig. 8(*a*)), indicating that because of the bending and straightening of wavy tow segments at the locations of tow crossovers, strain and stress concentrations arise; that is, this is highly heterogeneous dependent on the weave architecture in textile CMCs. The effects

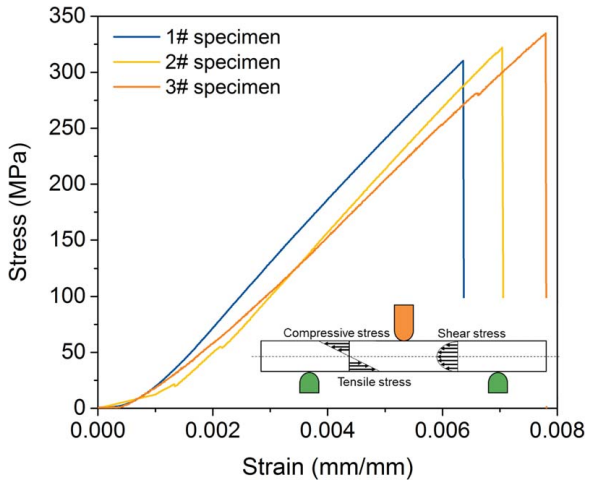

Fig. 6 Stress–strain curves of SiC/SiC CMC specimens tested using a three-point bend configuration at room temperature. Distinction between the different domains of the curves, namely, the first nonlinear part and the second quasi-linear part

are exacerbated by reductions in the constraints on bending and straightening caused by matrix damage, especially in surface plies. The tensile and compressive strains are symmetric along the neutral axis. As the flexural stress increases, the values of the tensile and compressive strains increase (Figs. 8(*b*)–8(*d*)). When the flexural stress reaches $0.8\sigma_u$, significant local strain concentrations are developed at the tensile surface (Fig. 8(*d*)) and become extremely inhomogeneous as the flexural stress reaches σ_u (Fig. 8(*f*)).

As for the materials under bending loading, both sides of the specimen are subjected to tensile and compressive loads separately; thus, there must be a transition axis on the cross section that is

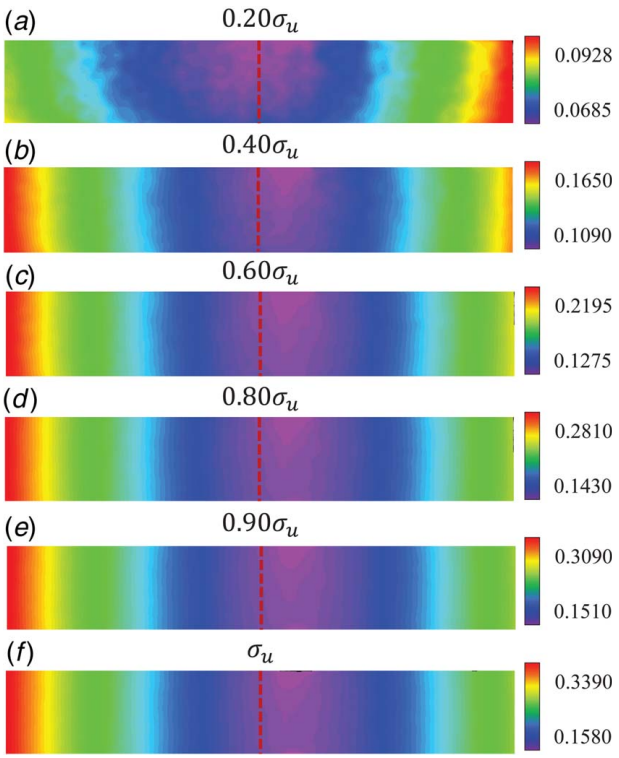

Fig. 7 Displacement fields of the specimen in the *XY* plane under different loadings, generated by DIC. The bending center is marked by dotted lines, which is the location of the loading pin.

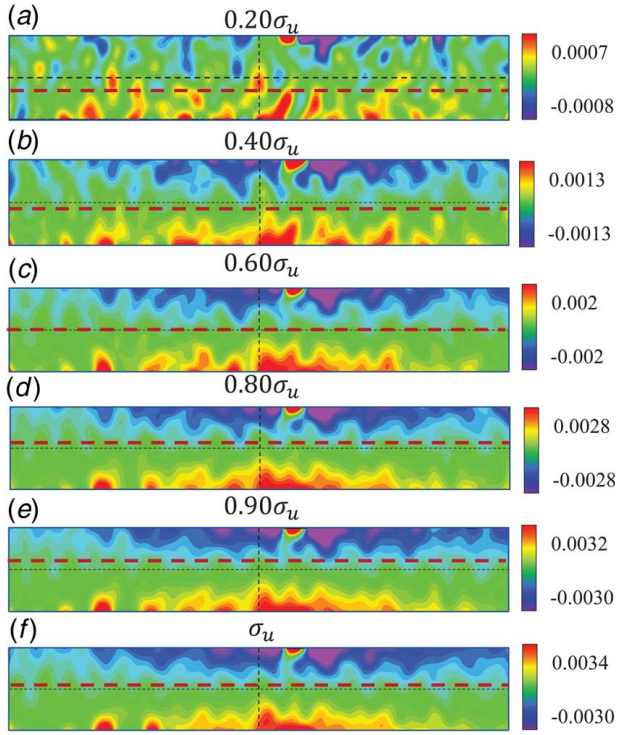

Fig. 8 Evolution of the flexural strain field ε_{xx} with increasing applied stress. The dotted lines represent the location of the loading pin.

neither stretched nor compressed, which indicates that the stress at this axis is almost equal to zero. This transition axis is named the neutral axis of the material. Interestingly, the neutral axis will change during the bending process, which reflects the different damage states of the material on the compression side and the tension side. As the obtained strain field is influenced by the laminated structure and the woven pattern of the composites, the region where the average strain in the thickness direction of the material is zero is defined as the neutral axis.

As shown in Fig. 8, when the flexure stress is below 0.2 σ_u, the neutral axis is below the centerline of the thickness, as the tensile modulus is higher than the compressive modulus of the SiC/SiC CMCs. As the flexural stress increases, the damage in the materials will generate a nonlinear strain distribution, and the neutral axis moves to the centerline, as the damage causes the tensile modulus to decrease at the surface. When the flexural stress is $0.6\sigma_u$, the neutral axis progressively moves from the beam center to close to the compressive surface. When the flexural stress reaches σ_u, the compressive side suffers damage, leading to a decrease in the modulus, and the neutral axis returns toward the centerline.

The effective elastic modulus of the SiC/SiC CMCs can be determined from the three-point bend flexure experiments based on the theory of Euler–Bernoulli beam [39]. Due to the inhomogeneous stress/strain distributions in composites, the movement of the neutral axis is neglected and assumes that the flexural strain varies linearly. Then, the effective elastic modulus of the specimen can be calculated by

$$\frac{1}{\rho} = \frac{\varepsilon_{xx}}{Y} = \frac{M}{EI} \tag{3}$$

where ρ is the curvature of the specimen, Y is the distance of the calculated point to the beam center, M is the change in the applied bending moment, I is the second moment of area of the beam, and E is the effective elastic modulus. Equation (3) can be easily used to estimate the effective elastic modulus with the results measured by DIC.

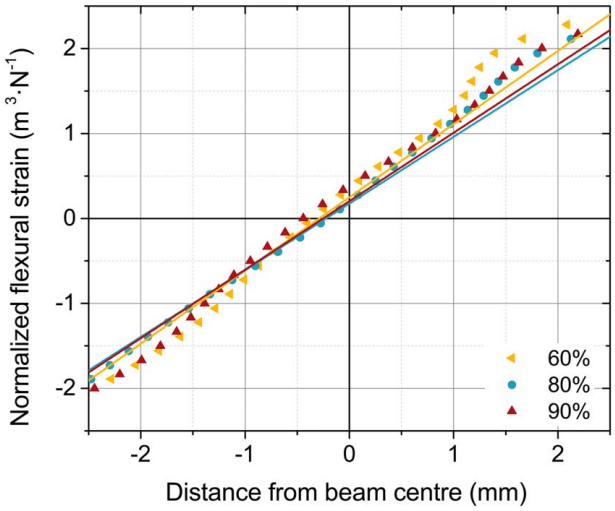

Fig. 9 Normalized strains ($\varepsilon_{xx}(I/M)$) along the direction of thickness (Y)

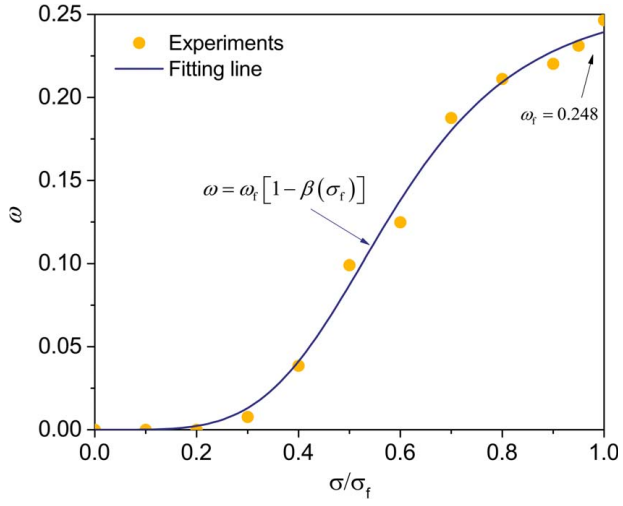

Fig. 11 Flexural loading-induced damage variation as a function of the applied stress for the SiC/SiC CMCs

The relationship between the normalized flexural strains, $\varepsilon_{xx}(I/M)$ M/I, and the distance Y is shown in Fig. 9, which can be described through a linear fit curve. The gradient of the fit curve provides the effective elastic modulus as a function of the applied stress.

Therefore, the effective elastic modulus of the SiC/SiC CMCs with the applied stress can be obtained as shown in Fig. 10. Due to matrix cracks, fiber fragmentation, and interface debonding and delamination on both the tensile side and compressive side of the specimens, the elastic modulus of the SiC/SiC CMCs decreases with increasing flexural loading. Similar results were reported by Liu et al. [29] for 3D four-step braided SiC/SiC CMCs, which are also plotted in Fig. 10. Regarding the present SiC/SiC CMCs, the elastic modulus decreases rapidly at 40% σ_u, and 40% σ_u is defined as a threshold for the flexural-induced damage, σ_{init}.

When the applied stress is less than the threshold value ($\sigma_u < \sigma_{init}$), E rarely changes, as there is little damage in the materials, and some cracks can be observed on the tensile surface. As the applied stress increases to σ_{init}, E drops rapidly because new matrix cracks, interface debonding, and fiber breakage take place dramatically. The elastic modulus is reduced from $0.95E_0$ to $0.75E_0$ at $0.9\sigma_u$, and damage occurs at the compressive surface.

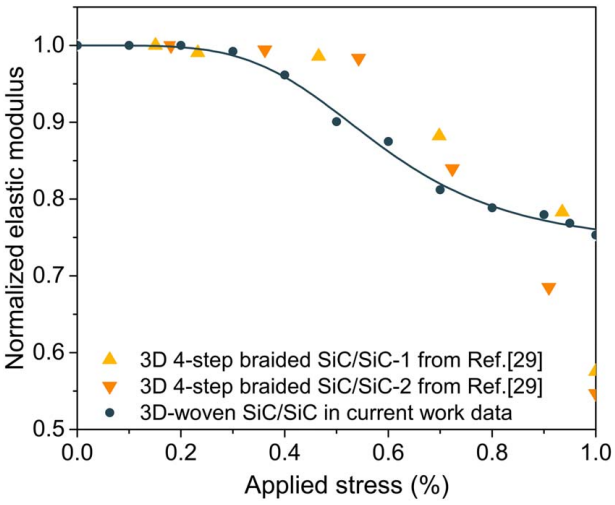

Fig. 10 The relationship between E and the applied stress and similar results were reported by Liu et al. [29] for 3D four-step braided SiC/SiC CMCs

Then, the value of E tends to be stable for a higher stress level, as the damages in the materials are gradually saturated.

The degradation of the elastic modulus of the SiC/SiC composite with applied loading can be described by an exponential function:

$$\tilde{E} = E_0 - E_f[1-\beta(\sigma)] \tag{4}$$

where $\tilde{E}$ represents the effective elastic modulus of the damaged materials, E_0 is the original elastic modulus, and E_f denotes the lowest elastic modulus when the material fails. $\beta(\sigma)$ is a dimensionless function of the applied flexural stress σ, and

$$\beta(\sigma) = \left(\frac{\sigma}{K}\right)^n \tag{5}$$

Here, n is a material mechanical resistance hardening/softening exponent, and K is the material mechanical resistance constant. Taking the logarithm of Eq. (4),

$$\ln\left(1-\frac{\tilde{E}-E_0}{E_f}\right) = \ln E_f + n\ln(\ln\sigma - \ln K) \tag{6}$$

By letting $x = \ln\sigma$ and $y = \ln\left(1-((\tilde{E}-E_0)/E_f)\right)$, the parameters K and n can be obtained. Equation (4) can be used to describe the relationship between E and the applied stress, as shown in Fig. 10, and the good fitting confirmed the reliability of the proposed equation.

3.3 Representation of Flexural Loading-Induced Damage.

Since the mechanical behaviors of the SiC/SiC CMCs are generally quasi-damageable-elastic, it is difficult to describe the major features of flexural loading-induced damage to the materials. The goal of this section is to establish a damage model to represent the damage caused by flexural loading.

According to the theory of continuum damage mechanics [40], the damage can be defined as the decrease in the elastic modulus, which is the phenomenological representation of the damage, and

$$\omega = 1 - \frac{\tilde{E}}{E_0} \tag{7}$$

where ω denotes the flexural loading-induced damage to the materials. Equation (7) connects the elastic modulus reduction with the material damage ω; then, the relationship between ω and the applied stress can be represented by Fig. 11.

To quantify the damage evolution with flexural load processing, the evolution of the damage can be obtained by combining Eqs. (4)

and (7):

$$\omega = \omega_f[1 - \beta(\sigma)] \tag{8}$$

where ω_f is the maximum damage when the materials fail, corresponding to E_f in Eq. (4). The function β has been defined in Eq. (5).

As shown in Fig. 11, the material damage starts from zero, and it should be noted that the as-received composites contain a large number of initial defects and microstructural damage because of their monolithic ceramic properties and high-temperature process characteristics, which are not considered here. Since the flexural loading is not increased to make the materials fracture, $\omega_f = 0.248$, which is less than 1, and ω_f can be considered a material-specific parameter.

4 Damage Evolution Formulation

There are great challenges in constructing damage models of SiC/SiC CMCs, as various damage mechanisms exist during flexural loading [41]. With these considerations, many researchers have developed micromechanics-based models to represent the realistic damage of materials physically [42–44]. However, such models have difficulty relating the microstructure damage to the macroscopic mechanical properties, as they are effective at the constituent scale of the materials. Consequently, in this section, a model based on CDM is established to quantitatively describe the flexural loading-induced damage of the SiC/SiC CMCs. The state of the damage within the composite is described by internal damage variables. As these damage variables evolve with the applied load, the stiffness of the composite is degraded. In addition, the damage evolution laws are calibrated using experimental data.

4.1 Thermodynamic Laws. To describe the damage behavior of the SiC/SiC CMCs under flexural loading, the Helmholtz free energy ψ is introduced with a set of internal state variables that can characterize the damage behaviors well as follows:

$$\psi = \psi^e\left(\varepsilon^e, \omega^+, \omega^-\right) = \frac{1}{2}\sigma_{ij}\varepsilon^e_{ij} \tag{9}$$

Here, the elastic behavior of the materials is considered, and ψ can be expressed as a decomposition of elastic ψ^e. ω^+ and ω^- are the accumulated damage variables due to tensile stress and compressive stress, respectively. It should be noted that during the flexural loading process, the materials can suffer both tensile and compressive damage, and these different types of damage can cause different irreversible microstructure changes, leading to the degradation of stiffness, as mentioned in Sec. 3.1. Equation (9) shows that the damage only affects the elastic property of the SiC/SiC CMCs under flexural loading.

In addition, the Clausius–Duhem inequality is expressed as

$$\sigma_{ij}\dot{\varepsilon}_{ij} - \rho\dot{\psi} \geqslant 0 \tag{10}$$

and ρ is the density of the materials.

Then, the stress in the material can be obtained as

$$\sigma_{ij} = \rho\frac{\partial\psi^e}{\partial\varepsilon^e_{ij}} = E_{ijkl}\varepsilon^e_{kl} \tag{11}$$

where E_{ijkl} is the stiffness matrix of the material.

By substituting Eq. (11) into Eq. (7), the effective stress tensor for the damaged material is given by

$$\tilde{\sigma}_{ij} = \frac{\sigma_{ij}}{1-\omega} \tag{12}$$

Then, by considering Eq. (12) and the linear isothermal isotropic elasticity, Eq. (9) can be expressed as

$$\rho\psi^e = \frac{1+\nu}{2E}\frac{\sigma^\omega_{ij}\sigma^\omega_{ij}}{1-\omega} + \frac{3(1-2\nu)}{2E}\frac{\sigma^2_H}{1-\omega} = \frac{\sigma^2_{eq}R_\nu}{2E(1-\omega)} \tag{13}$$

Here, $\sigma_H = \sigma_{kk}/3$ is the hydrostatic stress, and $\sigma_{eq} = \sqrt{\frac{3}{2}\sigma^\omega_{ij}\sigma^\omega_{ij}}$ denotes the von Mises equivalent stress. $\sigma^\omega_{ij} = \sigma_{ij} - \sigma_H\delta_{ij}$ is the deviatoric stress. The stress triaxiality R_ν can be used to denote the ratio σ_H/σ_{eq} as

$$R_\nu = \frac{2}{3}(1+\nu) + 3(1-2\nu)\left(\frac{\sigma_H}{\sigma_{eq}}\right)^2 \tag{14}$$

4.2 Formulation of the Damage Law. The damage evolution is governed by the associated variables; that is, the dissipative damage potential function is primarily a function of the energy density release rate, Y, based on the thermodynamics approach, and it can be derived from the state potential as

$$Y^\pm = \rho\frac{\partial\psi^e}{\partial\omega^\pm} = \frac{\tilde{\sigma}^2_{eq}R_\nu}{2E} \tag{15}$$

Then, the rate of the internal variables associated with damage deformations can be defined as

$$\dot{\omega}^\pm = \dot{\lambda}_d\frac{\partial F_D{}^\pm}{\partial Y^\pm} \tag{16}$$

where $F^\pm_D$ represents the potential function, which can be used to predict damage initiation and growth. $\dot{\lambda}_d$ is the damage Lagrangian multiplier, which is non-negative and characterized by the Kuhn–Tucker complementary conditions

$$F^D(Y^\pm, \omega^\pm) \leqslant 0$$

$$\dot{\lambda}_d F^D(Y^\pm, \omega^\pm) = 0$$

Then, it can be deduced that

$$\dot{F}^D(Y^\pm, \omega^\pm)\begin{Bmatrix} <0 \Rightarrow \dot{\lambda}_d = 0 \\ =0 \Rightarrow \dot{\lambda}_d = 0 \\ =0 \Rightarrow \dot{\lambda}_d > 0 \end{Bmatrix} \Leftrightarrow \begin{Bmatrix} \text{effective (undamaged state)} \\ \text{damage initiation} \\ \text{damage growth} \end{Bmatrix} \tag{17}$$

The potential function for the damage is defined by [45]

$$F^\pm_D = Y^\pm - R(\omega)^\pm \tag{18}$$

where $R(\omega)^\pm$ represents the material resistance against material damage. Only when the damage driving force $Y^\pm$ is greater than $R(\omega)^\pm$, will damage occur in the materials. Referring to Ref. [45], $R(\omega)$ can be obtained by

$$R(\omega)^\pm = Y^\pm_0\left[1 - \frac{1}{B^\pm}\ln\left(1-\omega^\pm\right)\right] \tag{19}$$

where $Y^\pm_0$ is the damage threshold, and $B^\pm$ is the material constant related to the fracture energy.

$\dot{\lambda}_d$ in Eq. (17) is determined under the following damage consistency condition:

$$dF^{D\pm} = \frac{\partial F^{D\pm}}{\partial Y^\pm}\dot{Y}^\pm - \frac{\partial R(\omega)^\pm}{\partial\omega^\pm}\dot{\lambda}_d = 0 \tag{20}$$

The rate form of the damage driving function Y can be expressed by taking the time derivative of Eq. (20):

$$\dot{Y}^\pm = \frac{Y_0{}^\pm}{B^\pm}\exp\left[-B^\pm\left(1 - \frac{Y^\pm}{Y_0}\right)\right]\dot{\omega}^\pm \tag{21}$$

Equation (21) describes the damage evolution with the energy density release rate Y for the SiC/SiC CMCs under flexural loading, and the model parameters B and Y_0 can be determined by fitting the experimental data.

Figure 12 shows the relationship between the damage and energy density release rate Y. There is nearly no damage when Y is less than the threshold value Y_0. At $Y > Y_0$, the damage shows a rapid

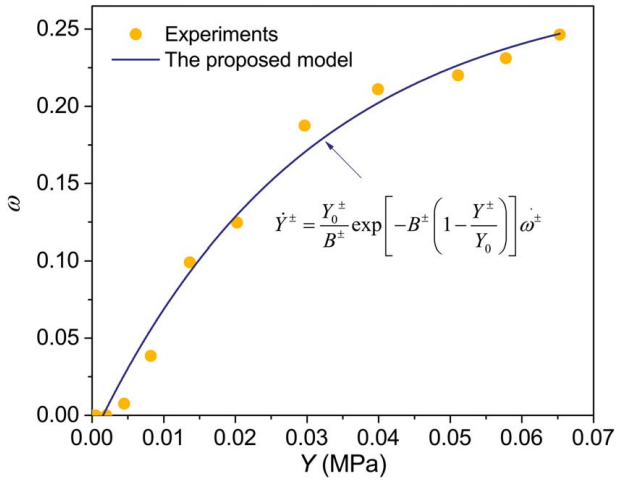

Fig. 12 Flexural loading-induced damage evolution with the energy density release rate *Y* for the SiC/SiC CMCs under flexural loading

increase. As Y increases, the damage reaches a saturation stage, and $\omega^{sat} = 0.25$ at $Y = 0.065$ MPa because the strain energy damage rate decreases gradually in the plane of the maximum principal stress.

5 Conclusions

In the present work, the microstructure deformation and its synergetic damage evolution of 3D textile SiC/SiC CMCs under flexural loading were investigated. During flexural loading, matrix cracking initially occurs on the tensile side, and its propagation is diffused into sinuous fractures and presents a zigzag path feature, which will not completely lose the loading capacity of the materials. With increasing flexural loading, the local stress concentration caused by the loading pin leads to both matrix cracking and interlayer debonding on the compressive side, which results in the ultimate failure of the materials. The ultimate failure of the specimen is caused by the damage extended from the compressive to the tensile surface. Besides, the effective elastic modulus of the composites is determined from three-point bend flexure experiments based on DIC measurements. E shows a rapid drop when the applied stress is higher than the threshold value due to the microstructure damage occurring dramatically. The reduction of the elastic modulus can be used to represent the phenomenological material damage.

With detailed experimental observations and DIC, the relationship between microstructure evolution and macro-mechanical degradation of 3D textile composites under flexural loading is generated by establishing the flexural loading-induced damage evolution model. Based on the CDM and thermodynamic theory, a synergetic damage evolution model is established to predict the effects of flexural loading-induced damage on the macroscopic material properties, and the model parameters can be identified through experiments. The excellent agreement between the model and experimental results shows that the proposed damage model can predict the mechanical properties of the 3D textile SiC/SiC CMCs under flexural loading, as well as to provide guidance for the textile architecture design of 3D textile composites.

Acknowledgment

The present work is supported by the National Natural Science Foundation of China (NSFC) (Grant No. 52105165) and the Strategic Priority Research Program of Chinese Academy of Sciences (Grant No. XDA17030100).

Conflict of Interest

There are no conflicts of interest.

Data Availability Statement

The authors attest that all data for this study are included in the paper.

References

[1] Padture, N. P., 2016, "Advanced Structural Ceramics in Aerospace Propulsion," Nat. Mater., **15**(8), pp. 804–809.
[2] Almansour, A. S., and Morscher, G. N., 2020, "Tensile Creep Behavior of SiC_F/SiC Ceramic Matrix Minicomposites," J. Eur. Ceram. Soc., **40**(15), pp. 5132–5146.
[3] Delage, J., Saiz, E., and Al Nasiri, N., 2022, "Fracture Behaviour of SiC/SiC Ceramic Matrix Composite at Room Temperature," J. Eur. Ceram. Soc., **42**(7), pp. 3156–3167.
[4] Yang, Z., Yuan, H., and Liu, H., 2019, "Evolution and Characterization of Cyclic Thermal Shock-Induced Thermomechanical Damage in Oxide/Oxide Ceramics Matrix Composites," Int. J. Fatigue, **120**, pp. 150–161.
[5] Dai, S., Cunningham, P. R., Marshall, S., and Silva, C., 2015, "Influence of Fibre Architecture on the Tensile, Compressive and Flexural Behaviour of 3D Woven Composites," Composites Part A: Appl. Sci. Manuf., **69**, pp. 195–207.
[6] Santhosh, U., Ahmad, J., Ojard, G., and Gowayed, Y., 2021, "A Synergistic Model of Stress and Oxidation Induced Damage and Failure in Silicon Carbide-Based Ceramic Matrix Composites," J. Am. Ceram. Soc., **104**(8), pp. 4163–4182.
[7] Gale, L., Harris, S., Pattison, S., Baker, J., and Fowler, J., 2021, "Development and Evaluation of Sub-element Testing of SiC/SiC Ceramic Matrix Composites at Elevated Temperatures," J. Eur. Ceram. Soc., **41**(5), pp. 3167–3176.
[8] Alabdullah, M., and Ghoniem, N. M., 2019, "Damage Mechanics Modeling of the Non-linear Behavior of SiC/SiC Ceramic Matrix Composite Fuel Cladding," J. Nucl. Mater., **524**, pp. 296–311.
[9] Chen, Y., Gélébart, L., Chateau, C., Bornert, M., Sauder, C., and King, A., 2019, "Analysis of the Damage Initiation in a SiC/SiC Composite Tube From a Direct Comparison Between Large-Scale Numerical Simulation and Synchrotron X-Ray Micro-computed Tomography," Int. J. Solids Struct., **161**, pp. 111–126.
[10] Poerschke, D. L., Rossol, M. N., and Zok, F. W., 2017, "Intermediate Temperature Oxidative Strength Degradation of a SiC/SiNC Composite With a Polymer-Derived Matrix," J. Am. Ceram. Soc., **100**(4), pp. 1606–1617.
[11] Song, C., Liu, Y., Ye, F., Cheng, L., Zhang, P., and Chai, N., 2021, "Enhanced Mechanical Property and Tunable Dielectric Property of SiCf/SiC-SiBCN Composites by CVI Combined With PIP," J. Adv. Ceram., **10**(4), pp. 758–767.
[12] Yang, Z., Sun, J., Yang, J., Liu, T., and Liu, H., 2022, "Mechanical Behavior of Woven CMCs Under Non-uniform Stress and Strain Fields," Compos. Struct., **299**, p. 116097.
[13] Callaway, E. B., and Zok, F. W., 2020, "Tensile Response of Unidirectional Ceramic Minicomposites," J. Mech. Phys. Solids, **138**, p. 103903.
[14] Swaminathan, B., McCarthy, N. R., Almansour, A. S., Sevener, K., Pollock, T. M., Kiser, J. D., and Daly, S., 2021, "Microscale Characterization of Damage Accumulation in CMCs," J. Eur. Ceram. Soc., **41**(5), pp. 3082–3093.
[15] Morscher, G. N., 2010, "Tensile Creep and Rupture of 2D-Woven SiC/SiC Composites for High Temperature Applications," J. Eur. Ceram. Soc., **30**(11), pp. 2209–2221.
[16] Mazars, V., Caty, O., Couegnat, G., Bouterf, A., Roux, S., Denneulin, S., Pailhes, J., and Vignoles, G. L., 2017, "Damage Investigation and Modeling of 3D Woven Ceramic Matrix Composites From X-Ray Tomography In-Situ Tensile Tests," Acta Mater., **140**, pp. 130–139.
[17] Hilmas, A. M., Sevener, K. M., and Halloran, J. W., 2020, "Damage Evolution in SiC/SiC Unidirectional Composites by X-Ray Tomography," J. Am. Ceram. Soc., **103**(5), pp. 3436–3447.
[18] Zhang, D., Liu, Y., Liu, H., Feng, Y., Guo, H., Hong, Z., Chen, C., and Zhang, Y., 2021, "Characterisation of Damage Evolution in Plain Weave SiC/SiC Composites Using In Situ X-Ray Micro-computed Tomography," Compos. Struct., **275**, p. 114447.
[19] Rajan, V. P., and Zok, F. W., 2012, "Effects of Non-uniform Strains on Tensile Fracture of Fiber-Reinforced Ceramic Composites," J. Mech. Phys. Solids, **60**(12), pp. 2003–2018.
[20] Rajan, V. P., and Zok, F. W., 2014, "Matrix Cracking of Fiber-Reinforced Ceramic Composites in Shear," J. Mech. Phys. Solids, **73**, pp. 3–21.
[21] Hild, F., Domergue, J., Leckie, F. A., and Evans, A. G., 1994, "Tensile and Flexural Ultimate Strength of Fiber-Reinforced Ceramic-Matrix Composites," Int. J. Solids Struct., **31**(7), pp. 1035–1045.
[22] McNulty, J. C., and Zok, F. W., 1997, "Application of Weakest-Link Fracture Statistics to Fiber-Reinforced Ceramic-Matrix Composites," J. Am. Ceram. Soc., **80**(6), pp. 1535–1543.
[23] Zhang, D., Waas, A. M., and Yen, C., 2015a, "Progressive Damage and Failure Response of Hybrid 3D Textile Composites Subjected to Flexural Loading, Part I: Experimental Studies," Int. J. Solids Struct., **75–76**, pp. 309–320.
[24] Zhang, D., Waas, A. M., and Yen, C., 2015b, "Progressive Damage and Failure Response of Hybrid 3D Textile Composites Subjected to Flexural Loading, Part

II: Mechanics Based Multiscale Computational Modeling of Progressive Damage and Failure," Int. J. Solids Struct., **75–76**, pp. 321–335.
[25] Yang, Y., Liu, X., Wang, Y., Gao, H., Li, R., and Bao, Y., 2017, "A Progressive Damage Model for Predicting Damage Evolution of Laminated Composites Subjected to Three-Point Bending," Compos. Sci. Technol., **151**, pp. 85–93.
[26] Chao, X., Qi, L., Tian, W., Hou, X., Ma, W., and Li, H., 2018, "Numerical Evaluation of the Influence of Porosity on Bending Properties of 2D Carbon/Carbon Composites," Compos. Part B Eng., **136**, pp. 72–80.
[27] Wan, F., Liu, R., Wang, Y., Cao, Y., Zhang, C., and Marrow, T. J., 2019, "Damage Development During Flexural Loading of a 5-Directional Braided C/C-SiC Composite, Characterized by X-Ray Tomography and Digital Volume Correlation," Ceram. Int., **45**(5), pp. 5601–5612.
[28] Pirzada, T. J., Liu, D., Ell, J., Barnard, H., Šulák, I., Galano, M., Marrow, T. J., and Ritchie, R. O., 2021, "In Situ Observation of the Deformation and Fracture of an Alumina-Alumina Ceramic-Matrix Composite at Elevated Temperature Using X-Ray Computed Tomography," J. Eur. Ceram. Soc., **41**(7), pp. 4217–4230.
[29] Liu, C., Chen, Y., Shi, D., Marrow, J., Jing, X., and Yang, X., 2021, "In Situ Investigation of Failure in 3D Braided SiC_f/SiC Composites Under Flexural Loading," Compos. Struct., **270**, p. 114067.
[30] Rajan, V. P., Rossol, M. N., and Zok, F. W., 2012, "Optimization of Digital Image Correlation for High-Resolution Strain Mapping of Ceramic Composites," Exp. Mech., **52**(9), pp. 1407–1421.
[31] Gonabadi, H., Oila, A., Yadav, A., and Bull, S., 2021, "Structural Performance of Composite Tidal Turbine Blades," Compos. Struct., **278**, p. 114679.
[32] Gonabadi, H., Oila, A., Yadav, A., and Bull, S., 2021, "Fatigue Damage Analysis of GFRP Composites Using Digital Image Correlation," J. Ocean Eng. Mar. Energy, **7**(1), pp. 25–40.
[33] Gonabadi, H., Oila, A., Yadav, A., and Bull, S., 2021, "Investigation of Anisotropy Effects in Glass Fibre Reinforced Polymer Composites on Tensile and Shear Properties Using Full Field Strain Measurement and Finite Element Multi-scale Techniques," J. Compos. Mater., **56**(3), pp. 507–524.
[34] Bumgardner, C. H., Heim, F. M., Roache, D. C., Price, M. C., Deck, C. P., and Li, X., 2021, "Characterizing Environment-Dependent Fracture Mechanisms of Ceramic Matrix Composites Via Digital Image Correlation," J. Am. Ceram. Soc., **104**(12), pp. 6545–6562.
[35] Yang, H., Zhou, X., Yu, J., Wang, H., and Huang, Z., 2015, "Microwave and Conventional Sintering of SiC/SiC Composites: Flexural Properties and Microstructures," Ceram. Int., **41**(9), pp. 11651–11654.
[36] ASTM C1341-13, 2013, "Standard Test Method for Flexural Properties of Continuous Fiber-Reinforced Advanced Ceramic Composites," ASTM International.
[37] Marshall, D. B., and Evans, A. G., 1985, "Failure Mechanisms in Ceramic-Fiber/Ceramic-Matrix Composites," J. Am. Ceram. Soc., **68**(5), pp. 225–231.
[38] Beyerle, D. S., Spearing, S. M., and Evans, A. G., 1992, "Damage Mechanisms and the Mechanical Properties of a Laminated 0/90 Ceramic/Matrix Composite," J. Am. Ceram. Soc., **75**(12), pp. 3321–3330.
[39] Eugster, S. R., 2015, *Geometric Continuum Mechanics and Induced Beam Theories*, Lecture Notes in Applied and Computational Mechanics, Springer International Publishing, Cham.
[40] Lemaitre, J., and Desmorat, R., 2005, *Engineering Damage Mechanics: Ductile, Creep, Fatigue and Brittle Failures*, Springer-Verlag, Berlin.
[41] Chateau, C., Gelebart, L., Bornert, M., Crepin, J., Caldemaison, D., and Sauder, C., 2014, "Modeling of Damage in Unidirectional Ceramic Matrix Composites and Multi-scale Experimental Validation on Third Generation SiC/SiC Minicomposites," J. Mech. Phys. Solids, **63**, pp. 298–319.
[42] Marcin, L., Maire, J., Carrère, N., and Martin, E., 2010, "Development of a Macroscopic Damage Model for Woven Ceramic Matrix Composites," Int. J. Damage Mech., **20**(6), pp. 939–957.
[43] Shojaei, A., Li, G. Q., Fish, J., and Lan, P. J., 2014, "Multi-scale Constitutive Modeling of Ceramic Matrix Composites by Continuum Damage Mechanics," Int. J. Solids Struct., **51**(23–24), pp. 4068–4081.
[44] Oddy, C., Ekh, M., and Fagerström, M., 2022, "Macroscale Modelling of 3d-Woven Composites: Elasto-plasticity and Progressive Damage," Int. J. Solids Struct., **250**, p. 111696.
[45] Cicekli, U., Voyiadjis, G. Z., and Abu Al-Rub, R. K., 2007, "A Plasticity and Anisotropic Damage Model for Plain Concrete," Int. J. Plast., **23**(10), pp. 1874–1900.